ACS OMEGA

http://pubs.acs.org/journal/acsodf

Article

Thermal History Mapping in Powder Bed Laser Sintering at the Micrometer Scale

François Rouzé l'Alzit,* Thierry Cardinal, Gérard L. Vignoles, Élise Bonnet, and Manuel Gaudon*

Cite This: *ACS Omega* 2022, 7, 42801−42808

Read Online

ACCESS | Metrics & More | Article Recommendations | Supporting Information

ABSTRACT: A thermal sensor was used to better understand parameters which influenced the interaction between a laser beam and a 0.5% Mn-doped $ZnAl_{2.2}O_4$ material, especially the laser defocusing parameter. The optical properties of the material depend on whether the Mn^{2+} ions occupy octahedral and/or tetrahedral sites depending on thermal history. A screen printing process is performed to obtain material thin films. Laser irradiation of the films was carried out (patterning 1 cm length single laser track) with different z defocusing heights. Luminescence properties around laser tracks led to the thermal history determination at the micrometer scale. It was shown that spatial thermal gradients defined at the micrometer scale perpendicularly to the borders of the laser tracks could be semiquantified for different z conditions. Laser defocusing leads to decrease thermal gradients as confirmed by thermal modeling studies.

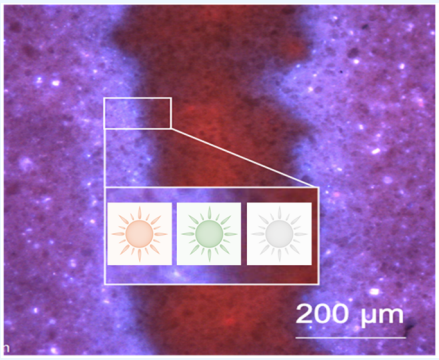

1. INTRODUCTION

Selective laser sintering (or herein, powder bed laser sintering: PBLS) is one of the new technologies belonging to the classification of additive manufacturing.[1] A laser beam sweeps a powder bed to sinter the material layer-by-layer, to obtain a 3D object.[2] This process depends on the thermal characteristics of the material and on a set of parameters of the device.[3] Focal length is one of these laser parameters to control the ceramic or metal sintering.[4−6] The main effect of defocusing is to reduce the reached temperatures.[7] Also, defocusing leads to an increase in the spot diameter, resulting in a higher sintering homogenization near the beam spot. This phenomenon could be used for sensitive ceramic materials. Indeed, in our precedent study,[8] we observed that cracks appear because high temperatures and especially high temperature gradients are both reached. A better understanding of the evolution of thermal gradients reached at the micrometric scale as a function of the laser defocusing parameter is required to optimize the laser sintering of ceramics.[9] The development of the shaping of ceramics by SLS technique requires a better understanding of the evolution of thermal gradients. In situ studies aimed at quantifying the spatial distribution of the temperature reached by the matter/laser interaction are very complex to carry out. Such experimental studies are also time-consuming due to the high number of key parameters to be evaluated. The observation and control of the temperature reached under laser radiation can be done using infrared thermal cameras which measure in real time the temperatures reached on the surface of the film in situ.[10−12] However, the precision of the camera, as well as its acquisition speed or the cost, limits its use in a generalized way.

We have therefore during our studies used two means of characterization, namely, the use of a digital model and the use of the ceramic material with thermo-chromoluminescence properties.

On one hand, modeling is an effective alternative to assess the temperatures reached during the process and how they are affected by different materials or laser parameters.[13] It predicts with relatively high accuracy the heat treatment regime that occurs during the experimental process of SLS. Modeling is based on the study of heat transfer within the material when it is subjected to laser radiation. There are three essential modes of heat transfer: conduction, radiation, and convection.[14] The description by robust thermodynamic equations of these three phenomena therefore makes it possible to formulate and calculate these temperatures and to obtain a map of the temperatures reached according to the parameters of the material and the laser. A large number of works use numerical models in parametric studies (whether laser parameter or material parameter) and compare the results from numerical models to experimental results. In the majority of cases, the experiments carried out on thermal conduction models in order to explore the thermal behavior during the SLM process concern metallic materials. Tolochko et al. studied the heat transfer mechanism induced by laser irradiation on titanium

Received: July 25, 2022
Accepted: November 3, 2022
Published: November 16, 2022

https://doi.org/10.1021/acsomega.2c04683
ACS Omega 2022, 7, 42801−42808

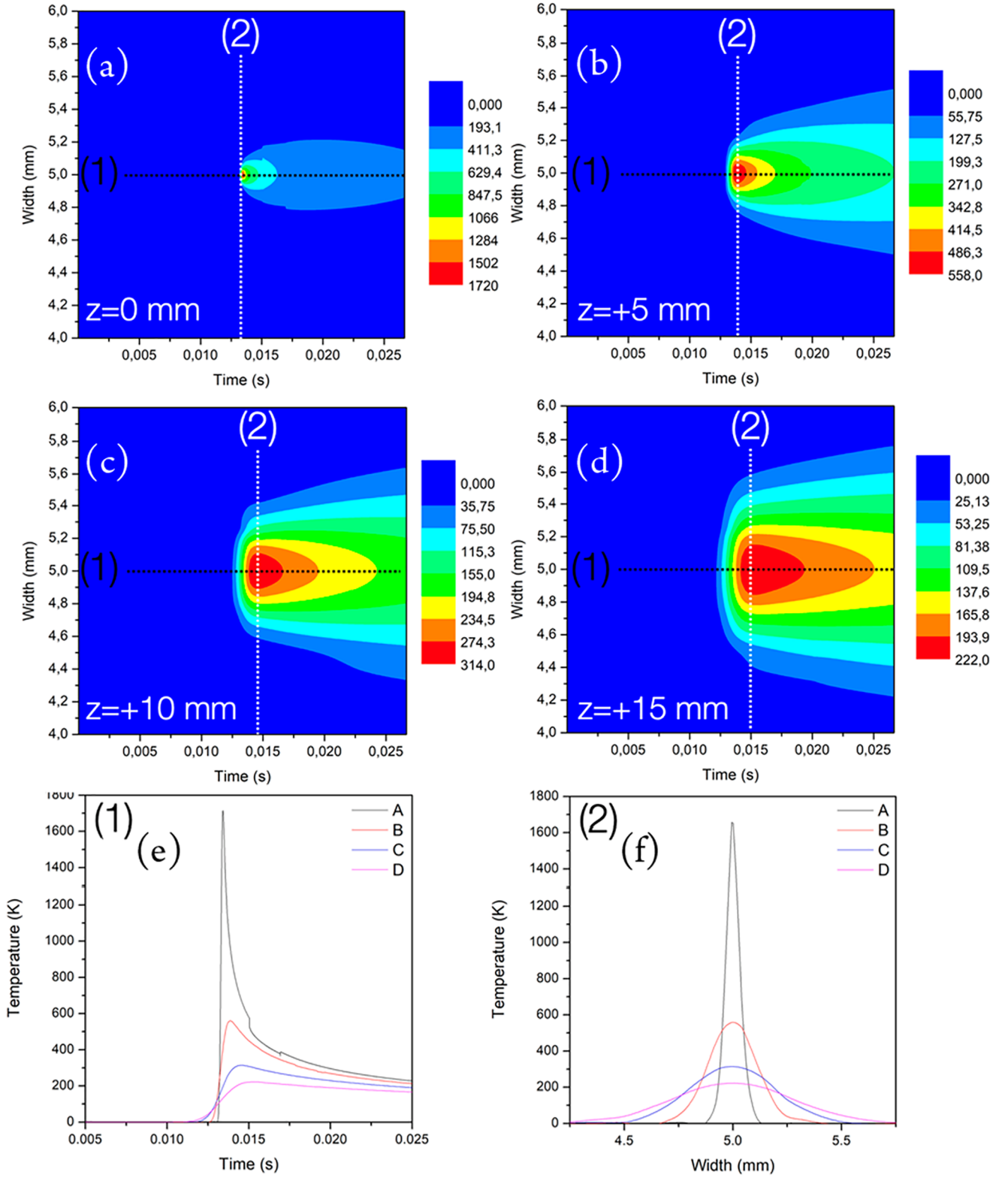

Figure 1. Thermal history mapping from modeling made with z focal height equal to 0 mm (a), 5 mm (b), 10 mm (c), and 15 mm (d). Thermal profile at the laser track central point as a function of time (e) and through the perpendicular axis of the laser track from this central point (f).

powder by coupling an experimental procedure and a heat transfer simulation.[15] Gusarov and Smurov used numerical methods to study the absorbance of a powder layer on different metals (Cu, Fe, Pb, Ti).[16] They confirmed that the absorbance of a powder bed is defined by a universal function of the absorptivity of the solid phase itself as a function of the wavelength and is independent of the morphology of the powder particles and the porosity of the powder bed. On the other hand, Li and Gu analyzed the thermal behavior during selective laser melting (SLM) of aluminum powder and

https://doi.org/10.1021/acsomega.2c04683
ACS Omega 2022, 7, 42801−42808

observed that the maximum temperature reached during the process is closely related to the film thickness and changes with the number of layers.[17] More recently, several authors have presented modeling results combined with experimental measurements on materials other than metals, such as polymers.[18−22] Concerning ceramic materials, only a few studies comparing numerical model/experimental results have been found in the literature. However, we can cite the work of Mahmood et al., who developed a mathematical model using MATLAB software to study the temperatures reached during laser sintering on a bulk substrate of silicon nitride (Si_3N_4) and on a alumina powder bed (Al_2O_3).[23] With their numerical model, they can predict the temperature distribution during the laser radiation−matter interaction with 8% accuracy. Thus, numerical modeling is appropriate to simulate the thermal diffusion inside metallic or polymer layers during the SLS process. Nevertheless, this technique faces significant challenges because this technique is dependent on a large number of parameters and remains under development for ceramic material.

On the other hand, in 2007, Christofferson et al. enumerated different methods for thermal micrometric characterization including liquid crystal thermography based on the crystalline phase change of a thin liquid crystal layer.[24] Most recently, Eickelmann et al. suggested to use alkanes to characterize temperature gradients at the micrometer scale.[25] Authors cast a thin alkane film onto the appropriate substrate and observed the evolution of the alkane film morphology by optical microscopy after the laser treatment to indirectly determine thermal gradients. These methods are adapted to quite low temperature only. Moreover, Choe et al. used an atomic-scale thermal sensor, e.g., the nitrogen vacancies in N-doped carbon diamond to try to obtain micrometric thermal maps.[26] Some authors have shown that it is possible to monitor the progress of laser heat treatment chirality-related properties on Ba−Ti−Cu phosphates.[27] Finally, another proposition is to use the thermo-chromoluminescent properties of smart thermal sensors. Several studies have shown the interest of thermo-chromoluminescent materials as thermal sensors.[28−32] Cornu et al. have studied the optical properties of Mn-doped $ZnAl_2O_4$, where the migration of manganese cations from an octahedral to a tetrahedral site affects the luminescence spectra with a change from red to green emission.[33] In our recent work, we have demonstrated that this material can be used to get an idea of the thermal history of thin ceramic films submitted to the PBLS process, for a temperature range between 800 and 1200 °C, i.e., at higher temperature than in the other solutions exposed in the literature.[34] Nevertheless, the spatial resolution of the temperature maps, especially the potentialities at the micrometer scale, still have to be better explored. Herein, we report the effect of laser defocusing parameter, especially its impact on thermal gradients at the micrometer scale on a ceramic film submitted to PBLS.

II. EXPERIMENTAL SECTION

As thermal sensing material, 0.5% Mn-doped $ZnAl_{2.2}O_4$ compound was chosen as the tested thin films over the PBLS process. The $Zn_{0.95}Mn_{0.05}Al_2O_4$ sample was synthesized by the Pechini route through a protocol already detailed in previous work.[34]

To perform the laser treatment, the powder was formed into a film on a glass substrate (insensitive to laser irradiation). A heat treatment was carried out in air, in the in-line form, with a continuous ytterbium laser at 1.07 μm (ES17-355, ES LASER). The 3 laser modulating parameters are the power (expressed as a percent of maximum power), the scanning speed (m s^{-1}), and the z focal length (mm).

The morphology of laser irradiated films (Figure 2) was observed thanks to an optical or scanning electron microscopy (SEM) (Leica DMI 3000 M enabling an excitation at 365 nm and a SEM-Jeol JSM-67).

The microluminescence spectra of the laser tracks were measured with a Labram 800-HR spectrophotometer (Horiba Jobin-Yvon) equipped with an Olympus microscope objective.

Laser defocusing was highlighted by a numerical analysis using a finite element solver. The modeling approach is focused on heat transfer from the laser to the film and from the film to its environment.[8] The model is restricted to a 2D depth-averaged model to record the surface temperatures reached upon laser heating which depend mainly on heat capacity (C_p), density (ρ), and thermal conductivity (k) of the material, but also on the transferred surface power from the laser to the film (Q_{laser}) and the air/film and air/substrate interface convective and radiative losses (H_l, detailed in ref 8), as depicted by the heat balance equation:

$$\rho C_p \frac{\partial T}{\partial t} = \mathrm{div}(k\nabla T) + Q_{laser} - H_l \quad (1)$$

The interaction of the laser beam and the surface of the powder bed induces a Gaussian distribution of intensity given by

$$Q_{laser}(x, y) = \frac{aP}{d\pi r^2} \exp\left(-\frac{x^2 + (y - vt)^2}{2r^2}\right) \quad (2)$$

with a being the material absorptivity, P the laser power (W), r the spot radius (m), d the laser penetration depth (m), and v the laser scanning speed in the y direction (m s^{-1}). All along the numerical experiments, all parameters are fixed at the exception of the laser defocusing length impacting the spot radius r.

III. RESULTS AND DISCUSSION

III.1. Modeling. Figure 1 shows the numerical modeling results of the impact of laser defocusing on the temperatures reached on the ceramic material. During this analysis, modeling the patterning of a 1 cm length single laser track, the software records the temperatures reached at a specific point (central point) and around this point as the laser beam moves over time (Supporting Information Figure S1). A broadening of the laser-affected zone—which is attributed to the diffusive propagation of heat—versus defocusing amplitude (z parameter) is observed (Figure 1a−d). Figure 1e also shows a significant decrease of the temperature curve slope when the laser is passing on the central point versus z (this is true for both the front curve associated with the temperature increase while the laser is approaching and the back curve associated with the temperature decrease while the laser is moving away). This clearly indicates a decrease of the temporal thermal gradients versus z. Similarly, Figure 1f shows a decrease in the slope of the temperature curves recorded orthogonally to the laser track around the central point.

Thus, defocusing allows thermal gradients both in time and space to be reduced. Therefore, our objective was to observe by experiment and at a micrometric scale how spatial thermal gradients are depending on the laser defocusing height (z).

https://doi.org/10.1021/acsomega.2c04683
ACS Omega 2022, 7, 42801−42808

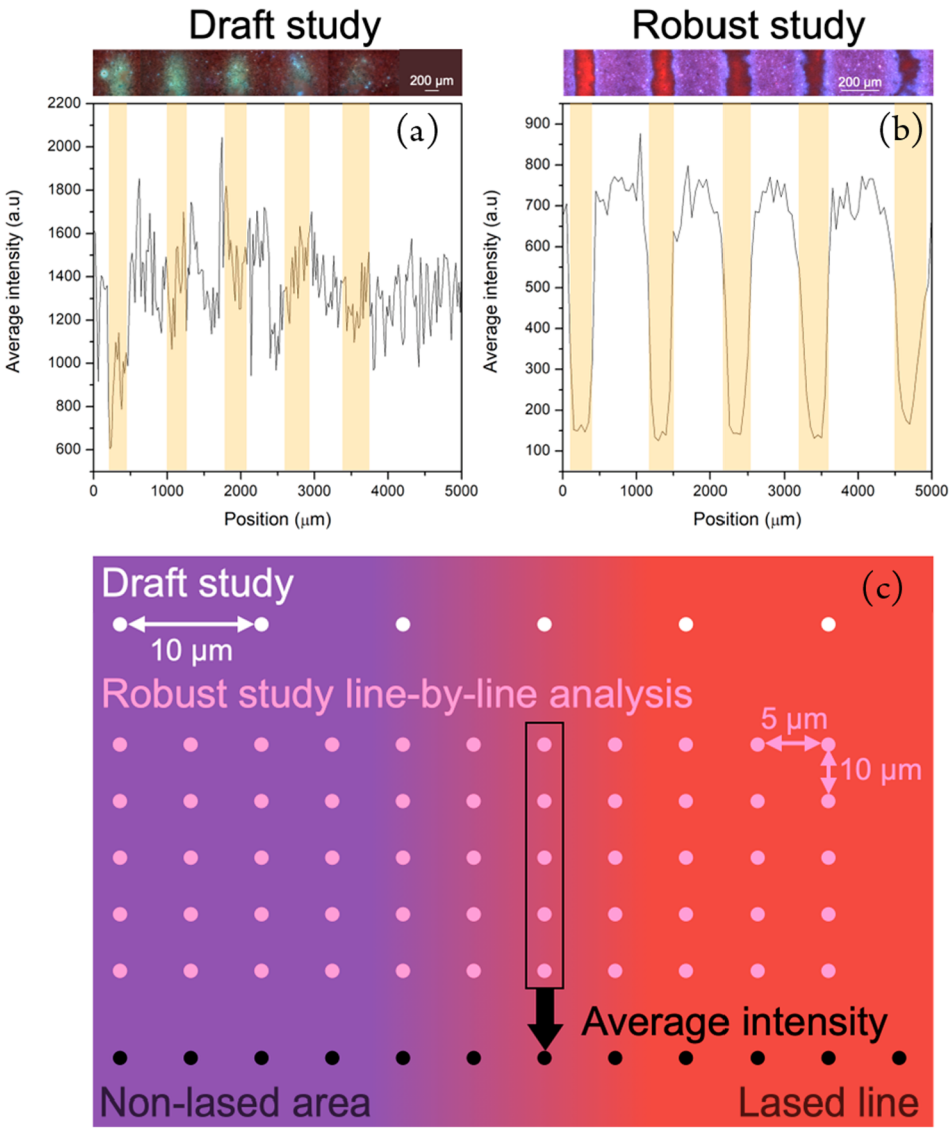

Figure 2. Red emission (analyzed by microluminescence) versus x position of the test points on spinel films width 5 laser tracks using different z heights for the draft (a) and robust study (b). Schemes of the draft versus the robust study (c).

The emphasis was set on the thermal history distribution perpendicularly to the laser track (i.e., depending on the x position, x axis corresponding to the perpendicular axis of each laser track).

III.2. Experimental Measures. On the Mn-doped $ZnMnAl_2O_4$ thin films, as thermal sensors, thermal history distribution perpendicularly to 5 laser tracks made with increasing z defocusing height between each line (z between 9 and 13 mm; 1 mm step) was determined. First, a draft study was made, assessing the laser effect from the red emission of spots distributed through the x axis with 10 μm spacing between 2 successive points. The spinel powder film was deposited on silica glass substrate by the doctor blade process. The powder was dispersed in ethanol (30−35 wt %) and ultrasonicated. The as-prepared viscous suspension was then coated to obtain a film thickness of about 40−50 μm, adjusted thanks to the razor blade. The red emission intensity (i.e., the average emission intensity calculated in the range from 705 to 725 nm) is a signal with high noise, which was associated with poor film quality as highlighted by SEM images (Figure S2b). To optimize the accuracy of the acquisition process, the quality of the film was improved using a more efficient deposition technique, namely, the screen printing process. This process requires specific inks, made of a mix of powders, binder (ethylcellulose), dispersant (Terpineol), and solvent (from DuPont). The total solid fraction in the ink was 36 wt %. The ink was put through a three-cylinder mill to obtain a fine and homogeneous particle dispersion, ready for the screen printing process which was performed with a screen printer Aurel C890. 50 μm thick films were obtained on an aluminate substrate by deposition of successive layers dried 1 min at 120 °C after each printing step and finally annealed at 600 °C for 4 h to remove organic compounds. SEM investigations showed a better film homogeneity (Figure S2c) with a structural framework, retaining a pure spinel form (Figure S2d). Then, on this new film, a robust laser study was performed by multiplying the analysis points: now with 5 μm step width. Furthermore, the intensity for each of the same x coordinate points (i.e., at the same distance from the laser track center) was calculated from the average intensity of 5 parallel analysis

https://doi.org/10.1021/acsomega.2c04683
ACS Omega 2022, 7, 42801−42808

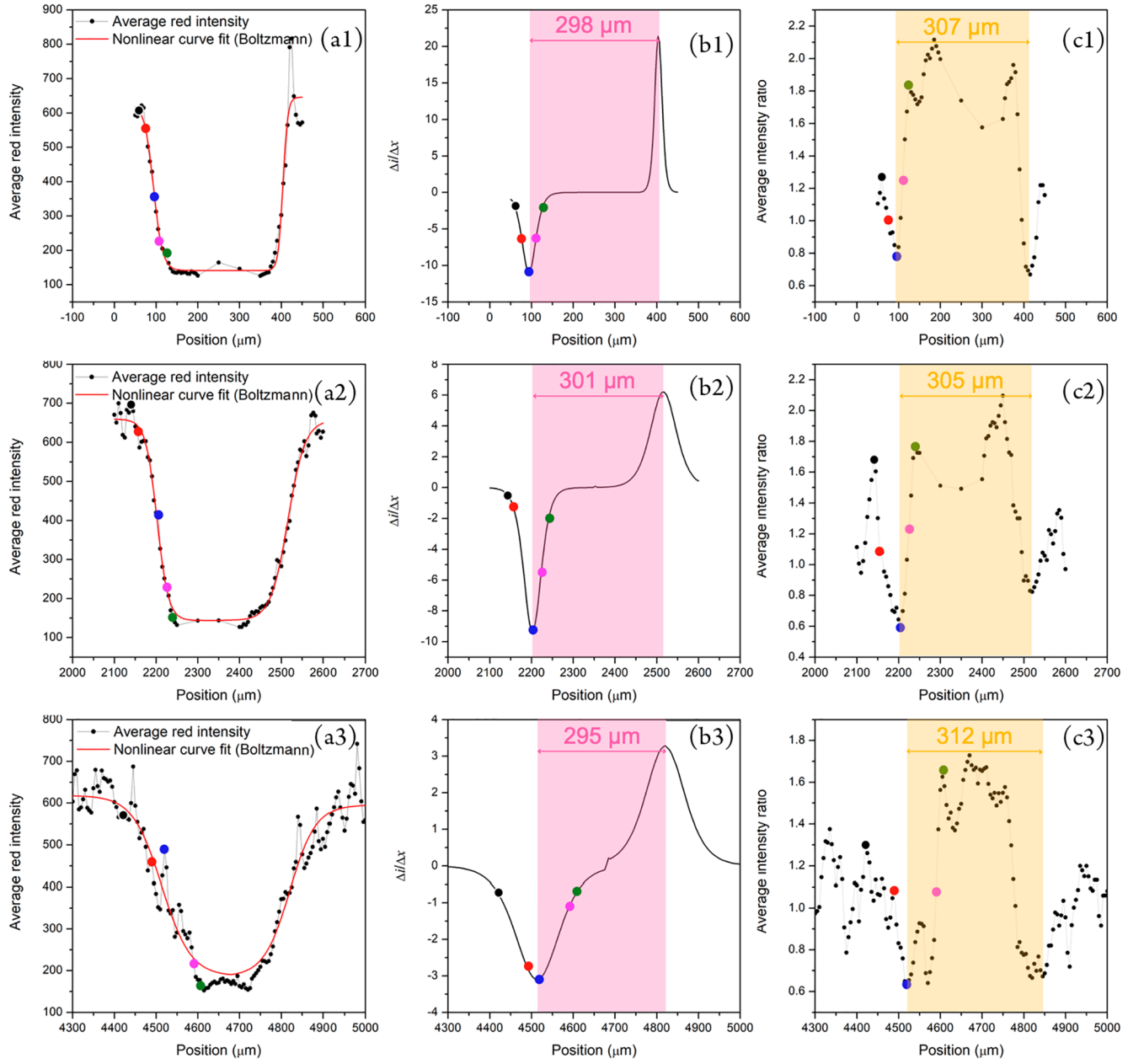

Figure 3. Study of luminescence through (versus x) 3 laser tracks. Average intensity of red luminescence and Boltzmann fit (a), derivative of the Boltzmann fit (b), and red/green emission intensity ratio. The pink and yellow strips represent the width extracted from derivative curve inflection points or two "blue spots" corresponding to red/green emission ratio minima (c).

lines. Figure 2b shows distinctly two different red emission intensity levels: (i) outside the laser track, the red emission intensity is high; (ii) inside the laser track, the red emission intensity is low. At the laser exposed/non-exposed interface, the red emission intensity varies abruptly. The phenomenon is the same whatever the 5 patterned lines with different defocusing conditions. Therefore, the optimizations of both the film manufacturing process and the acquisition process do allow a better discrimination of the red emission intensity depending on the laser surface power received by the material. Obviously, the multiplication of the analysis points, now in great number, deserves a robust and automatized numerical treatment.

Figure 3 describes the results of microluminescence analysis for the robust study on 3 laser tracks plotted using 9, 11, and 13 mm z defocusing heights, respectively. The first column's pictures (Figure 3a) correspond to the average of red emission intensity previously discussed. A fit of the intensity variation versus the x position around the laser track center is carried out, and its x derivative is expressed by the second column's picture (Figures 3b). Finally, the ratio of the red emission intensity over the green one is depicted in the third column's picture (Figures 3c). To help the interpretation, 3 different critical test spots (plus 2 intermediate test spots) are reported on each curve; these critical spots correspond to 3 luminescence regimes, i.e., three temperatures reached during the laser scanning process. For these 3 laser tracks, the full emission spectra recorded on the 3 critical + 2 intermediate spots (following the x axis from the outside to the center of each line: black, red, blue, pink, and green spots) are reported

https://doi.org/10.1021/acsomega.2c04683
ACS Omega 2022, 7, 42801−42808

in Figure S3. (i) "Outside" the laser track (upstream of the black point), the red emission intensity is high and associated with a red/green ratio higher than 1 remaining more or less stable: the black test point is chosen at the x position until, from the outside to the center of each laser track, a maximal and stable red emission intensity is observed. Mn^{2+} remains predominantly located into the octahedral sites of the spinel network. Therefore, upstream from this black point, the material has not undergone any significant thermal treatment. (ii) "Inside" the laser track (beyond the critical green spot) the red emission intensity is low and associated with a flat profile of the derivative curve (as well as with a high and constant red/green ratio), this corresponding to the higher thermal history (Figure S3). Therefore, it can be supposed that high temperature could promote an oxidation of manganese + II ions, which produces a luminescence extinction, as previously shown.[16] (iii) At the interface between these two extreme temperatures regimes, i.e., at the irradiated/nonirradiated area interface, the red emission intensity abruptly decreases, while the red/green emission ratio is showing an inflection toward a minimal value (where it is chosen to place the third critical blue point). Luminescence spectra at the blue point show major green emission intensity, meaning that Mn^{2+} cations are predominantly located inside the tetrahedral sites in the spinel crystalline network (Figure S3). Therefore, we conclude that thermal treatment decreases from the blue point to the black point, thus highlighting from the Δx between these two critical points, the thermal gradient amplitude. Also, this gradient amplitude can be extracted from the slope of the intensity curve at the inflection point. The three $\Delta I/\Delta x$ maxima are equal to ~12, 9.5, and 3.5 for the lines with z equal to 9, 11, and 13 mm, respectively (Figure 3b). This well illustrates the decrease of the temperature gradient at the border of the laser track increasing the laser defocusing. Additionally, these derivative maxima are roughly with the same positions as the blue spots (minima of the red/green emission ratios). So we have two estimates, leading to about the same results, which can be considered as the spatial limit of the laser track and so allow the line width extraction. From the laser track border identification (the width being extracted, from red intensity evolution, as in between the two derivative inflection points, pink stripe on Figure 3b; or from red/green emission ratio evolution, in between the two blue spots, yellow stripe in Figure 3c), it can be observed that the laser track width remains constant while the focal length and thus the spot size increase. This could suggest that the temperature range where the material is significantly modified is not impacted by the defocusing, which seems to be paradoxical since thermal gradients are less violent with the defocusing increase.

III.3. Comparison between Models and Experiences. The latter observations can be related to Figure 4. Theoretically, the laser beam intensity profile is considered Gaussian (Figure 4a) which allows the spot size to be calculated as a function of focal length. Figure 4b shows a continuous increase in theoretical diameter spot versus z defocusing height. However, when the theoretical spot diameter is compared to the as-extracted experimental widths, a difference between the curves is noted (Figure 4d), the experimental widths remaining constant, whereas the theoretical spot diameter increases versus z. Two phenomena could explain this effect, as shown by our modeling. First, the laser spot is a heat source including the intensity as a Gaussian function depending on diameter spot. Defocusing leads to an

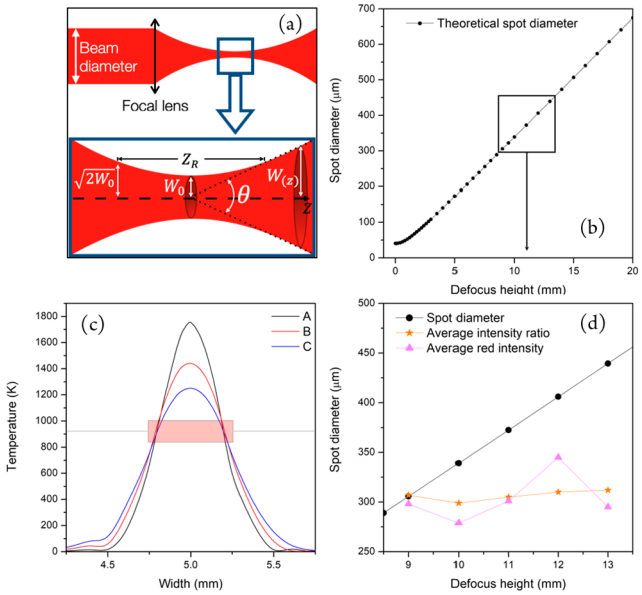

Figure 4. Theoretical laser spot diameter versus z: laser scheme (a) and calculation results (b). Modeled thermal profile versus x (orthogonally to the laser track) for the 3 different z heights (c). Comparison of theoretical and experimental laser track widths (d).

increase in the diameter spot, and consequently the Gaussian intensity dispersion spreads out (Figure 4c). In the same time, the boundaries between irradiated and nonirradiated areas become blurred with defocusing through a decrease of the temperature gradients. These two conjugated phenomena, maximum temperature decrease and temperature gradient decrease versus defocusing amplitude, lead to a crossing of the temperature curves reached during lasing (Figure 4c). Certainly, the critical points well marked by luminescence evolutions versus x are not so far from the zone where these temperature curves are crossing. Moreover, it is not so obvious, contrary to what was a priori assumed that an increase in spot diameter would lead to a decrease of the temperatures reached at the center of the laser track. Indeed, increasing the spot diameter leads to a decrease the laser intensity received per unit area by the irradiated material film; nonetheless, the increase of the spot size leads to an increase of the irradiation time. These opposite phenomena, maintaining the flux intensity received by the film from the laser, could also explain the apparently paradoxical constant width of the laser tracks versus z.

IV. CONCLUSION

In conclusion, a temperature-sensitive $Zn_{0.95}Mn_{0.05}Al_2O_4$ powder ink was realized to make film on alumina substrate as thermal history probes. Thermal treatments using laser located above the film with different focal lengths (z) were realized. The evolution of luminescence of the laser tracks as a function of z shows that the thermal gradients occurring at the micrometer scale at the borders of the laser tracks could be semiquantified for direct comparison between lines lased under different conditions. The thermal gradients are well spread out with z. Likewise, the laser tracks width appears quite independent of z, due to a combination of irradiated area spread and of a central temperature decrease while z increases. Experimental results are supported by the modeling of thermal profiles plotted perpendicularly to the laser tracks versus z. To

https://doi.org/10.1021/acsomega.2c04683
ACS Omega 2022, 7, 42801−42808

manage the temperature effects produced from laser irradiation is one of the most important elements to reach a better control of powder bed laser sintering, especially on ceramics, which are fragile and high melting point materials exposed to rapid crack propagation, limiting direct sintering.

Hence this work showing that the impact of the material parameters or the laser parameters on both the temporal gradients (kinetics of rise in temperature or of descent in temperature during the passage of the laser) and the spatial gradients (in particular temperature gradients around the laser point) could be accurately assessed is of great importance for the additive manufacturing community. The better understanding of the impact of the laser defocusing opens up new possibilities that would be developed on other ceramics such as bioceramics: hydroxyapatite, zirconia which will be mixed with the Mn-doped zinc aluminates used as thermal probe material.

■ ASSOCIATED CONTENT

Supporting Information

The Supporting Information is available free of charge at https://pubs.acs.org/doi/10.1021/acsomega.2c04683.

Heating effect at a central laser track point (Figure S1); thermal sensor structure (spinel network), phase purity (XRD), and morphology (SEM) (Figure S2); evolution studied from confocal microscopy of the emission spectra (Figure S3) (PDF)

■ AUTHOR INFORMATION

Corresponding Authors

Manuel Gaudon − *CNRS, Université de Bordeaux, Bordeaux INP, ICMCB (UMR 5026), Pessac F-33600, France;* orcid.org/0000-0002-6918-2004; Email: manuel.gaudon@icmcb.cnrs.fr

François Rouzé l'Alzit − *CNRS, Université de Bordeaux, Bordeaux INP, ICMCB (UMR 5026), Pessac F-33600, France*; Email: francois.rouze-l-alzit@u-bordeaux.fr

Authors

Thierry Cardinal − *CNRS, Université de Bordeaux, Bordeaux INP, ICMCB (UMR 5026), Pessac F-33600, France;* orcid.org/0000-0002-3008-8352

Gérard L. Vignoles − *Université de Bordeaux, CNRS, CEA, Safran: LCTS (UMR5801), Pessac F-33600, France*

Élise Bonnet − *CNRS, Université de Bordeaux, Bordeaux INP, ICMCB (UMR 5026), Pessac F-33600, France*

Complete contact information is available at: https://pubs.acs.org/10.1021/acsomega.2c04683

Notes

The authors declare no competing financial interest.

■ ACKNOWLEDGMENTS

We thank Alexandre Fargues, Sonia Buffièr,e and Jean-Marc Bassat for their assistance during microluminescence analysis, SEM analysis, and the screen printing process, respectively. We acknowledge the Nouvelle Aquitaine region for financial support (2016-1R10107).

■ REFERENCES

(1) Kumar, S.*Additive Manufacturing Processes*, 1st ed.; Springer: Cham, Switzerland, 2020. DOI: 10.1007/978-3-030-45089-2.

(2) Gibson, I.; Rosen, D.; Stucker, B.*Additive Manufacturing Technologies: 3D Printing, Rapid Prototyping, and Direct Digital Manufacturing*; Springer-Verlag: New York, 2015. DOI: 10.1007/978-1-4939-2113-3.

(3) Yadroitsev, I.; Bertrand, Ph.; Smurov, I. Parametric analysis of the selective laser melting process. *Appl. Surf. Sci.* **2007**, *253*, 8064−8069.

(4) Bertrand, Ph.; Bayle, F.; Combe, C.; Goeuriot, P.; Smurov, I. Ceramic components manufacturing by selective laser sintering. *Appl. Surf. Sci.* **2007**, *254*, 989−992.

(5) Bahador, A.; Hamzah, E.; Kondoh, K.; Abubakar, T.; Yusof, F.; Saud, S. N.; Ibrahim, M.; Ezazi, M. A. Defocusing Effects of Laser Beam on the Weldability of Powder Metallurgy Ti-Based Shape Memory Alloys. *Procedia Eng.* **2017**, *184*, 205−13.

(6) Khademzadeh, S.; Parvin, N.; Bariani, P. F.; Mazzucato, F. Effects of micro laser sintering process parameters on quality of nickel-titanium single tracks and thin walls. *Met. Mater. Int.* **2015**, *21*, 1081−1090.

(7) Lambiase, F.; Genna, S. Homogenization of temperature distribution at metal-polymer interface during Laser Direct Joining. *Opt. Laser Technol.* **2020**, *128*, 106226.

(8) Rouzé l'Alzit, F.; Bazin, T.; Cardinal, T.; Chung, U.-C.; Catros, S.; Bertrand, C.; Gaudon, M.; Vignoles, G. L. Powder Bed Laser Sintering of Copper-Doped Hydroxyapatite: Numerical and Experimental Parametric Analysis. *Addit. Manuf.* **2021**, *46*, 102044.

(9) Kim, S. S.; Armstrong, P. R.; Mah, M. L.; Talghader, J. J. Depth-dependent temperature effects on thermoluminescence in multilayers. *J. Appl. Phys.* **2013**, *114*, 053519.

(10) Wroe, W. W.; Gladstone, J.; Phillips, T.; Fish, S.; Beaman, J.; McElroy, A. In-situ thermal image correlation with mechanical properties of nylon-12 in SLS. *Rapid Prototyping J.* **2016**, *22*, 794−800.

(11) Bierwisch, C.; Mohseni-Mofidi, S.; Dietemann, B.; Grünewald, M.; Rudloff, J.; Lang, M. Universal process diagrams for laser sintering of polymers. *Mater.Des.* **2021**, *199*, 109432.

(12) Li, C.; Snarr, S. E.; Denlinger, E. R.; Irwin, J. E.; Gouge, M. F.; Michaleris, P.; Beaman, J. J. Experimental parameter identification for part-scale thermal modeling of selective laser sintering of PA12. *Addit. Manuf.* **2021**, *48*, 102362.

(13) Papazoglou, E. L.; Karkalos, N. E.; Karmiris-Obratański, P.; Markopoulos, A. P. On the Modeling and Simulation of SLM and SLS for Metal and Polymer Powders: A Review. *Arch. Computat. Methods Eng.* **2022**, *29*, 941−73.

(14) Dong, L.; Makradi, A.; Ahzi, S.; Remond, Y. Three-dimensional transient finite element analysis of the selective laser sintering process. *J. Mater. Process. Technol.* **2009**, *209*, 700−706.

(15) Tolochko, N. K.; Arshinov, M. K.; Gusarov, A. V.; Titov, V. I.; Laoui, T.; Froyen, L. Mechanisms of selective laser sintering and heat transfer in Ti powder. *Rapid Prototyping J.* **2003**, *9*, 314−326.

(16) Gusarov, A. V.; Smurov, I. Radiation transfer in metallic powder beds used in laser processing. *J. Quant. Spectrosc. Radiat. Transfer* **2010**, *111*, 2517−2527.

(17) Li, Y.; Gu, D. Parametric analysis of thermal behavior during selective laser melting additive manufacturing of aluminum alloy powder. *Materials & Design* **2014**, *63*, 856−67.

(18) Peyre, P.; Rouchausse, Y.; Defauchy, D.; Régnier, G. Experimental and numerical analysis of the selective laser sintering (SLS) of PA12 and PEKK semi-crystalline polymers. *J. Mater. Process. Technol.* **2015**, *225*, 326−36.

(19) Mokrane, A.; Boutaous, M.; Xin, S. Process of selective laser sintering of polymer powders: Modeling, simulation, and validation. *C. R. Mec.* **2018**, *346*, 1087−1103.

(20) Xin, L.; Boutaous, M.; Xin, S.; Siginer, D. A. Numerical modeling of the heating phase of the selective laser sintering process. *Int. J. Therm. Sci.* **2017**, *120*, 50−62.

(21) Xin, L.; Boutaous, M.; Xin, S.; Siginer, D. A. Multiphysical modeling of the heating phase in the polymer powder bed fusion process. *Addit. Manuf.* **2017**, *18*, 121−135.

(22) Riedlbauer, D.; Drexler, M.; Drummer, D.; Steinmann, P.; Mergheim, J. Modelling, simulation and experimental validation of heat transfer in selective laser melting of the polymeric material PA12. *Comput. Mater. Sci.* **2014**, *93*, 239−48.
(23) Mahmood, M. A.; Popescu, A. C.; Oane, M.; Ristoscu, C.; Mihailescu, I. N. Laser additive manufacturing of bulk and powder ceramic materials: mathematical modeling with experimental correlations. *Rapid Prototyping J.* **2022**, *28*, 1520−1529.
(24) Christofferson, J.; Maize, K.; Ezzahri, Y.; Shabani, J.; Wang, X.; Shakouri, A.*1st International Conference on Thermal Issues in Emerging Technologies, Theory and Applications; Proceedings−THETA1*, Cairo, Egypt, Jan. 3−6, 2007.
(25) Eickelmann, S.; Ronneberger, S.; Zhang, J.; Paris, G.; Loeffler, F. F. Alkanes as Intelligent Surface Thermometers: A Facile Approach to Characterize Short-Lived Temperature Gradients on the Micrometer Scale. *Adv. Mater. Interfaces.* **2021**, *8*, 2001626.
(26) Choe, S.; Yoon, J.; Lee, M.; Oh, J.; Lee, D.; Kang, H.; Lee, C. H.; Lee, D. Precise temperature sensing with nanoscale thermal sensors based on diamond NV centers. *Curr. Appl. Phys.* **2018**, *18*, 1066−1070.
(27) Hayashida, T.; Kimura, K.; Kimura, T. Switching Crystallographic Chirality in $Ba(TiO)Cu_4(PO_4)_4$ by Laser Irradiation. *J. Phys. Chem. Lett.* **2022**, *13*, 3857−3862.
(28) Rabhiou, A.; Feist, J.; Kempf, A.; Skinner, S.; Heyes, A. Phosphorescent thermal history sensors. *Sens. Actuators, A* **2011**, *169*, 18−26.
(29) Salek, G.; Demourgues, A.; Jubera, V.; Garcia, A.; Gaudon, M. Mn^{2+} doped $Zn_3(PO_4)_2$ phosphors: Irreversible thermochromic materials useful as thermal sensors. *Opt. Mater.* **2015**, *47*, 323−327.
(30) Cornu, L.; Gaudon, M.; Jubera, V. $ZnAl_2O_4$ as a potential sensor: variation of luminescence with thermal history. *J. Mater. Chem. C* **2013**, *1*, 5419−5428.
(31) Xiong, J.; Zhao, M.; Han, X.; Cao, Z.; Wei, X.; Chen, Y.; Duan, C.; Yin, M. Real-time micro-scale temperature imaging at low cost based on fluorescent intensity ratio. *Sci. Rep.* **2017**, *7*, 41311.
(32) Wang, J.-X.; Peng, L.-Y.; Liu, Z.-F.; Zhu, X.; Niu, L.-Y.; Cui, G.; Yang, Q.-Z. Tunable Fluorescence and Afterglow in Organic Crystals for Temperature Sensing. *J. Phys. Chem. Lett.* **2022**, *13*, 1985−1990.
(33) Cornu, L.; Duttine, M.; Gaudon, M.; Jubera, V. Luminescence switch of Mn-Doped $ZnAl_2O_4$ powder with temperature. *J. Mater. Chem. C* **2014**, *2*, 9512−9522.
(34) Rouzé l'Alzit, F.; Bazin, T.; Poulon-Quintin, A.; Champion, E.; Bertrand, C.; Cardinal, T.; Mjejri, I.; Rougier, A.; Jubera, V.; Gaudon, M. Thermochromoluminescent Mn^{2+}-Doped oxides as thermal sensor for selective laser sintering. *Opt. Mater.* **2020**, *110*, 110542.

https://doi.org/10.1021/acsomega.2c04683
ACS Omega 2022, 7, 42801−42808